38th Fluid Dynamics Conference and Exhibit
23 - 26 June 2008, Seattle, Washington

AIAA 2008-4059

High Order Conservative Differencing for Viscous Terms and the Application to Vortex-Induced Vibration Flows

Yiqing Shen*, Gecheng Zha†, Xiangying Chen
Dept. of Mechanical and Aerospace Engineering
Miami Wind^{TM}
University of Miami
Coral Gables, Florida 33124
E-mail: yqshen@miami.edu, gzha@miami.edu

Abstract

A set of conservative 4th-order central differencing schemes for the viscous terms of Navier-Stokes equations are proved in this paper. These schemes are used with the 5th order WENO schemes for inviscid flux. The stencil width of the central differencing scheme is within that of the WENO scheme. The algorithm is used to simulate the vortex-induced oscillations of an elastically mounted circular cylinder. The numerical results agree favorably with the experiment.

1 Introduction

High-order (higher than 2nd order) finite differencing algorithms have attracted more and more interest recently due to the increased demand to accurately predict engineering problems and understand fundamental flow physics[1, 2]. For example, the direct numerical simulations (DNS) of turbulence and aeroacoustics requires high order discretization schemes with low diffusion to resolve different scale turbulence eddies and acoustic propagation. Fluid-structure interaction flows also require low numerical dissipation in order to accurately predict the flow damping and structure response.

High-order accuracy requires high order evaluation of both the inviscid and viscous fluxes. However, most of the research focus on the inviscid fluxes to resolve discontinuities. For example, the essentially non-oscillatory (ENO) scheme[3, 4] and weighted essentially non-oscillatory (WENO) scheme[5, 6, 7, 8, 9] are all aimed at resolving the inviscid fluxes with high order accuracy in smooth regions and having the capability to capture shock wave and contact discontinuities.

To capture those discontinuities, the hyperbolic equations need to be solved in a conservative manner. A conservative numerical discretization is also essential to satisfy the conservation laws of fluid physics. A finite volume method based on the integral form of Navier-Stokes equations has the advantage to naturally obtain the conservation. For finite differencing method, a derivative needs to be discretized using the interface location between two solution points in order to be conservative.

For example, the following is a conservative finite differencing scheme.

* Research Scientist, AIAA Member
† Associate Professor, AIAA Senior Member

$$\frac{\partial f}{\partial x}_i = \frac{f_{i+1/2} - f_{i-1/2}}{\Delta x} \tag{1}$$

If the function $f_{i+1/2}$ is reconstructed with higher than 2nd order accuracy, Eq. 1 will give at least a 2nd order accuracy scheme.

For 2nd order accuracy schemes, there is not much difference for the computational amount between a finite volume or finite differencing scheme. However, for high order schemes, it is very different. As pointed out in references [10, 11], when the piece-wise parabolic reconstruction is used in two space dimensions, the finite volume WENO schemes require approximately three times more CPU time than the corresponding finite difference WENO schemes. In three space dimensions, the difference is about nine times. Hence, for the structured meshes, the finite difference WENO schemes are preferred. For the inviscid fluxes, the finite difference WENO schemes only need to handle first order derivatives. The WENO reconstruction ensures a conservative discretization of the first order derivatives. To match the stencil width of a WENO scheme, it is desirable to design a conservative central differencing scheme whose stencil width will be within that of the WENO scheme.

However, for the viscous fluxes that contain the 2nd order derivatives, such as

$$\frac{\partial}{\partial x}(\mu\frac{\partial f}{\partial x}) \quad or \quad \frac{\partial}{\partial x}(\mu\frac{\partial f}{\partial y}), \tag{2}$$

where μ is the viscosity coefficient, achieving a finite differencing scheme with both high order accuracy and conservativeness is not trivial. Most often, the 2nd order derivatives is achieved first by a high order differencing of the first order derivatives, and then the similar differencing scheme is applied again to obtain the high order 2nd order derivatives. These methods include the standard high order finite differencing schemes directly discretized on the node points and the compact schemes[12].

If a finite difference scheme is used, the high order approximation of the first order derivatives can be obtained first, and then substitute them to Eq. (1) to achieve a conservative differencing for the 2nd order derivatives. If the viscosity coefficient is constant, the conservative high-order schemes are straitforward and simple, for example, a fourth-order discretization can be constructed by using five points. However, if the viscosity coefficient is variable as in compressible flows, the conservative high order finite differencing schemes for those viscous terms are not obvious. A conservative finite differencing scheme for the cross derivatives are even more complicated.

For example, if a standard central difference scheme is used, the discretizations for a 2nd order derivative will involve a large number of grid points with a wide stencil. For example, for fourth-order accuracy, the following discretization will have

$$\frac{\partial}{\partial x}(\mu\frac{\partial f}{\partial x})|_i = \frac{1}{\Delta x}\sum_{k=-2}^{k=2}\beta_k\mu_{i+k}\frac{\partial f}{\partial x}|_{i+k} + O(\Delta x^4) \tag{3}$$

and

$$\frac{\partial f}{\partial x}|_l = \frac{1}{\Delta x}\sum_{k=-2}^{k=2}\beta_k f_{l+k} + O(\Delta x^4) \tag{4}$$

where β_k are the constant coefficients to make Eqs. (3) and (4) satisfied. So that these grid points $(f_{i+4}, f_{i+3}, \cdots, f_{i-4})$ are involved in Eq.(3). The stencil width of the fourth-order viscous terms is hence greater than that of the fifth-order WENO schemes, in which the stencil of width is $(f_{i+3}, f_{i+2}, \cdots, f_{i-3})$.

De Rango and Zingg[13] and Zingg et al[14] constructed a 4th order accuracy conservative scheme for the viscous terms. However, their schemes do not achieve the maximum order accuracy within the stencil

width used. In addition, they do not have conservative finite differencing schemes to treat the 2nd order cross derivatives.

The purpose of this paper is to employ a set of reconstruction formula to achieve fully conservative 4th order accuracy finite differencing schemes for all the 2nd order derivatives viscous terms of Navier-Stokes equations in generalized coordinates. Such conservative schemes are essential to be used with the conservative 5th order WENO schemes to enhance the overall accuracy of the flow solutions. The 4th order schemes studied in this paper are first presented in [15]. This paper gives the proof. The constraints we set are that the stencil width to evaluate these conservative 2nd order derivatives will not be greater than that of the WENO scheme. This set of formulations appears to be the first complete set of fully conservative 4th order finite differencing schemes for the viscous terms.

The other special numerical technique used in this paper is that the solution points are not located at the grid nodes as a standard finite differencing method. Instead, they are shifted by half a grid interval from the grid nodes in every direction. In this way, they are exactly located at the center of a grid cell in the generalized coordinates. In physical domain, they may not be in the center of a cell. There are two very useful advantages of this treatment: 1) it is straightforward to impose accurate boundary conditions such as no slip conditions. 2) the grid cell interfaces are the location to evaluate the conservative flux or derivative reconstruction. It hence allows a direct use of the computer code structure of a low order finite volume code with the solution points located in the center of the cells.

1.1 Application to vortex-induced vibration flows

The practical significance of vortex-induced vibrations of basic fluid dynamics and engineering applications has led to a large number of experimental and numerical investigations. Sarpkaya[16] and Williamson and Govardhan [17, 18] gave comprehensive overviews on the vortex-induced vibration flows (VIV). Al Jamal and Dalton [19] reviewed recent numerical studies on VIV of a circular cylinder and investigated the irregular behavior of the phase angle. An overview is also given for the numerical methods used in solving the fully coupled fluid-structure interaction problem by Gabbai and Benaroya[20].

Various CFD methods are employed to study the vortex-induced vibration flows, including the Reynolds Averaged Navier-Stokes (RANS) methods, Large Eddy Simulations (LES), Direct Numerical Simulations (DNS), and their various combinations. DNS are usually restricted to a low Reynolds number. LES has been used to solve the problem at moderate and high Reynolds numbers. Meynen et al.[21] used the 2nd order finite volume method with a central differencing scheme and the Crank-Nicholson scheme. Mittal and Kumar[22, 23, 24] used the space-time finite element approach and Blackburn et al[25, 26] used spectral element-Fourier spatial discretion method to solve the incompressible NS equations. DNS based on spectral element method is used in Refs.[27, 28, 29]. Beam-Warming central difference scheme is employed to solve the compressible NS equations[30]. Spectral-element method[31] and second-order Monotone Advection and Reconstruction Scheme [32] were employed to solve incompressible Navier-Stokes equations. The second-order consistent physical interpolation (CPI) approach is used to solve the 2D unsteady NS equations by Guilmineau and Queutey [33, 34] and the third-order upwind difference scheme QUICK is applied to solve the SST k-ϵ turbulence model by Pan et al.[35]. The LES method with the finite element code[36] and with the standard second-order finite difference scheme[19, 37] are also used. Chen and Zha[38, 39] developed a fully coupled fluid-structural interaction method, in which the 3rd order MUSCL differencing for inviscid fluxes and 2nd order central differencing for viscous terms are used. Except the spectral method, the differencing schemes in the aforementioned research work are all at 2nd order accuracy.

In this paper, the 5th order accuracy WENO scheme for the inviscid fluxes and the 4th order fully conservative central differencing for the viscous terms are used to simulate the cylinder flows due to vortex-induced cylinder vibration. The WENO scheme is used to obtain the shock capturing capability to prepare for the future transonic fluid-structural interaction simulation. Since there are no shock discontinuities in

the cylinder flows, the WENO scheme is fixed to its optimum weights to achieve minimum dissipation. The fully coupled fluid-structural interaction strategy developed by Chen and Zha[38, 39] is employed.

2 Numerical Methods

2.1 Flow Governing Equations

The normalized Navier-Stokes equations governing compressible viscous flows can be written in the Cartesian coordinate as:

$$\frac{\partial Q}{\partial t}+\frac{\partial E}{\partial x}+\frac{\partial F}{\partial y}+\frac{\partial G}{\partial z}=\frac{1}{Re}\left(\frac{\partial R}{\partial x}+\frac{\partial S}{\partial y}+\frac{\partial T}{\partial z}\right) \tag{5}$$

$$Q=\begin{bmatrix}\rho\\ \rho u\\ \rho v\\ \rho w\\ \rho e\end{bmatrix},\ E=\begin{bmatrix}\rho u\\ \rho u^2+p\\ \rho uv\\ \rho uw\\ (\rho e+p)u\end{bmatrix},\ F=\begin{bmatrix}\rho v\\ \rho uv\\ \rho v^2+p\\ \rho vw\\ (\rho e+p)v\end{bmatrix},\ G=\begin{bmatrix}\rho w\\ \rho uw\\ \rho vw\\ \rho w^2+p\\ (\rho e+p)w\end{bmatrix},$$

$$R=\begin{bmatrix}0\\ \tau_{xx}\\ \tau_{xy}\\ \tau_{xz}\\ u_k\tau_{xk}-q_x\end{bmatrix},\ S=\begin{bmatrix}0\\ \tau_{xy}\\ \tau_{yy}\\ \tau_{yz}\\ u_k\tau_{yk}-q_y\end{bmatrix},\ T=\begin{bmatrix}0\\ \tau_{xz}\\ \tau_{yz}\\ \tau_{zz}\\ u_k\tau_{zk}-q_z\end{bmatrix},$$

The repeated index k stands for the Einstein summation over x, y and z. The stress τ and heat flux q are,

$$\tau_{ik}=\mu\left[(\frac{\partial u_i}{\partial x_k}+\frac{\partial u_k}{\partial x_i})-\frac{2}{3}\delta_{ik}\frac{\partial u_j}{\partial x_j}\right]$$

$$q_j=\frac{-\mu}{(\gamma-1)M_\infty^2 Pr}\frac{\partial T}{\partial x_j}$$

The equation of state is

$$\rho e=\frac{p}{\gamma-1}+\frac{1}{2}\rho(u^2+v^2+w^2)$$

In the above equations, ρ is the density, u, v, and w are the Cartesian velocity components in x, y and z directions, p is the static pressure, and e is the total energy per unit mass, μ is the molecular viscosity, J is the transformation Jacobian, γ, Re, M_∞ *and* Pr are the ratio of specific heat, Reynolds number, Mach number and Prandtl number, respectively.

In the generalized coordinates, Eq.(5) can be written as:

$$\frac{\partial Q'}{\partial t}+\frac{\partial E'}{\partial \xi}+\frac{\partial F'}{\partial \eta}+\frac{\partial G'}{\partial \zeta}=\frac{1}{Re}\left(\frac{\partial R'}{\partial \xi}+\frac{\partial S'}{\partial \eta}+\frac{\partial T'}{\partial \zeta}\right) \tag{6}$$

where,

$$Q'=\frac{1}{J}Q,$$

$$E' = \frac{1}{J}(\xi_t U + \xi_x E + \xi_y F + \xi_z G),$$
$$F' = \frac{1}{J}(\eta_t U + \eta_x E + \eta_y F + \eta_z G),$$
$$G' = \frac{1}{J}(\zeta_t U + \zeta_x E + \zeta_y F + \zeta_z G),$$
$$R' = \frac{1}{J}(\xi_x R + \xi_y S + \xi_z T),$$
$$S' = \frac{1}{J}(\eta_x R + \eta_y S + \eta_z T),$$
$$T' = \frac{1}{J}(\zeta_x R + \zeta_y S + \zeta_z T).$$

For simplicity, the prime $'$ in Eq.(6) will be omitted.

It was pointed out by Thomas and Lombard[40] that, due to the mixed temporal and spatial derivatives after discretization, an additional term appears, which theoretically equals zero, but numerically still remains. Consequently, numerical error could be introduced in the discretized form of the equations of the flow motion if this term is neglected. In order to reduce or avoid this error, the geometric conservation law needs to be enforced. In other words, the following additional term should be added to the right-hand side of the equations as a source term:

$$\mathbf{S} = \mathbf{Q}\left[\frac{\partial J^{-1}}{\partial t} + \left(\frac{\xi_t}{J}\right)_\xi + \left(\frac{\eta_t}{J}\right)_\eta + \left(\frac{\zeta_t}{J}\right)_\zeta\right] \tag{7}$$

2.2 The 5th-Order WENO Scheme[5]

The finite difference 5th-order accuracy WENO scheme suggested by Jiang and Shu [5] is used for the inviscid flux. The fifth-order accurate WENO ($r = 3$) reconstruction of u^L can be written as

$$u^L_{i+1/2} = \omega_0 q_0 + \omega_1 q_1 + \omega_2 q_2$$

where

$$q_0 = \frac{1}{3}u_{i-2} - \frac{7}{6}u_{i-1} + \frac{11}{6}u_i$$
$$q_1 = -\frac{1}{6}u_{i-1} + \frac{5}{6}u_i + \frac{1}{3}u_{i+1}$$
$$q_2 = \frac{1}{3}u_i + \frac{5}{6}u_{i+1} - \frac{1}{6}u_{i+2}$$

and

$$\omega_k = \frac{\alpha_k}{\alpha_0 + \cdots + \alpha_{r-1}},$$
$$\alpha_k = \frac{C_k}{\varepsilon + IS_k}, \quad k = 0, \cdots, r-1$$

$$C_0 = 0.1, \quad C_1 = 0.6, \quad C_2 = 0.3$$
$$IS_0 = \frac{13}{12}(u_{i-2} - 2u_{i-1} + u_i)^2 + \frac{1}{4}(u_{i-2} - 4u_{i-1} + 3u_i)^2$$
$$IS_1 = \frac{13}{12}(u_{i-1} - 2u_i + u_{i+1})^2 + \frac{1}{4}(u_{i-1} - 4u_i + 3u_{i+1})^2$$

$$IS_2 = \frac{13}{12}(u_i - 2u_{i+1} + u_{i+2})^2 + \frac{1}{4}(u_i - 4u_{i+1} + 3u_{i+2})^2$$

where, ε is introduced to avoid the denominator becoming zero. In the practical applications, ε plays an important role on the convergence, stability and accuracy of WENO scheme [15, 41]. The higher the ε value, the closer for the weights to the optimum value C_k, and hence the lower the numerical dissipation. However, when there is a shock in the flow, the ε value can not be too large to maintain the sensitivity to the shock. In [15], $\varepsilon = 10^{-2}$ is recommended for the transonic flows with shock waves. In this paper, since there is no shock wave in the flow, we use the fixed weights $\omega_k = C_k$ to have minimum numerical dissipation.

The u^R is constructed symmetrically as u^L about $i + 1/2$.

2.3 The Discretization of Viscous Terms[15]

A set of fully conservative fourth-order accurate finite central differencing schemes for the viscous terms is suggested in this paper. These central differencing schemes are constructed so that the stencil widths are within the one of the WENO scheme. We take the viscous flux derivative in ξ-direction as the example to explain how the schemes are constructed.

To conservatively discretize the viscous derivative term in Navier-Stokes equations Eq.(6), we have

$$\frac{\partial R}{\partial \xi}|_i = \frac{\tilde{R}_{i+1/2} - \tilde{R}_{i-1/2}}{\Delta\xi} \tag{8}$$

To obtain 4th order accuracy, $\tilde{R}$ needs to be reconstructed as

$$\tilde{R}_{i-1/2} = \sum_{I=i-3/2}^{i+1/2} \alpha_I R_I \tag{9}$$

where

$$\begin{aligned}
&\alpha_{i-3/2} = -\frac{1}{24},\ \alpha_{i-1/2} = \frac{26}{24},\ \alpha_{i+3/2} = -\frac{1}{24} \\
&R_{i-1/2} = \left[(\xi_x\tau_{xx}) + (\eta_y\tau_{xy}) + (\zeta_z\tau_{xz})\right]_{i-1/2} \\
&(\tau_{xx}) = \ \mu\{\tfrac{4}{3}\left[(\xi_x\tfrac{\partial u}{\partial \xi}) + (\eta_x\tfrac{\partial u}{\partial \eta}) + (\zeta_x\tfrac{\partial u}{\partial \zeta})\right] \\
&\qquad -\tfrac{2}{3}[(\xi_y\tfrac{\partial v}{\partial \xi}) + (\eta_y\tfrac{\partial v}{\partial \eta}) + (\zeta_y\tfrac{\partial v}{\partial \zeta}) \\
&\qquad (\xi_z\tfrac{\partial w}{\partial \xi}) + (\eta_z\tfrac{\partial w}{\partial \eta}) + (\zeta_z\tfrac{\partial w}{\partial \zeta})]\}
\end{aligned} \tag{10}$$

If R in Eq.(9) can be approximated with the accuracy order not lower than 4th order, the Taylor series expansion analysis of (8) and (9) will give

$$\frac{1}{\Delta\xi}(\tilde{R}_{i+1/2} - \tilde{R}_{i-1/2}) = R^{'}(\xi_i) + O(\Delta\xi^4) \tag{11}$$

and the 4th order accuracy is achieved (to be proved later). It needs to point out that in Eq.(8), $\tilde{R}_{i-1/2}$ can not be replaced by $R_{i-1/2}$. Otherwise, the 4th order accuracy can not be achieved even though the high order approximation of $R_{i-1/2}$ is used. The 4th order accuracy from Eq. (8)-(11) is also based on the uniform spacing $\Delta\xi = C$.

In order to achieve the highest order accuracy of R_I with $I = i-3/2, i-1/2, i+1/2$, the approximation of each term in Eq. (9) using the same points is given below:

$$\mu_I = \sum_{l=m}^{n} C_l^I \mu_{i+l}, \tag{12}$$

$$\frac{\partial u}{\partial \xi}|_I = \frac{1}{\Delta \xi} \sum_{l=r}^{s} D_l^I u_{i+l}, \tag{13}$$

$$\frac{\partial u}{\partial \eta}|_I = \sum_{l=m}^{n} C_l^I \frac{\partial u}{\partial \eta}|_{i+l,j} \tag{14}$$

where

$$\frac{\partial u}{\partial \eta}|_{i,j} = \frac{1}{\Delta \eta} \sum_{l=p}^{q} C_l^c u_{i,j+l}, \tag{15}$$

By choosing different ranges for $(m,n),(r,s),(p,q)$ and different coefficients C_l^I, D_l^I, C_l^c, one can obtain different order accuracy approximation to the viscous terms. The principle of choosing $(m,n),(r,s),(p,q)$ is to ensure that the approximation of $\frac{\partial R}{\partial \xi}|_i$ in Eq.(8) is a central differencing. For example, in this paper, $(m,n)=(-2,1),(r,s)=(-3,2), and\ (p,q)=(-2,2)$ are used, and they give

$$\mu_I = \sum_{l=m}^{n} C_l^I \mu_{i+l} + O(\Delta \xi^4), \tag{16}$$

$$\frac{\partial u}{\partial \xi}|_I = \frac{1}{\Delta \xi} \sum_{l=r}^{s} D_l^I u_{i+l} + O(\Delta \xi^5), \tag{17}$$

$$\frac{\partial u}{\partial \eta}|_I = \sum_{l=m}^{n} C_l^I \frac{\partial u}{\partial \eta}|_{i+l,j} + O(\Delta \xi^4, \Delta \eta^4), \tag{18}$$

where

$$\frac{\partial u}{\partial \eta}|_{i,j} = \frac{1}{\Delta \eta} \sum_{l=p}^{q} C_l^c u_{i,j+l} + O(\Delta \eta^4) \tag{19}$$

the coefficients C_l^I, D_l^I, C_l^c can be obtained by Taylor's series expansion and are given in Tables 1-3. For example,

$$\begin{cases} \mu_{i-3/2} = \frac{1}{16}(5\mu_{i-2} + 15\mu_{i-1} - 5\mu_i + \mu_{i+1}) + O(\Delta \xi^4) \\ \mu_{i-1/2} = \frac{1}{16}(-\mu_{i-2} + 9\mu_{i-1} + 9\mu_i - \mu_{i+1}) + O(\Delta \xi^4) \\ \mu_{i+1/2} = \frac{1}{16}(\mu_{i-2} - 5\mu_{i-1} + 15\mu_i + 5\mu_{i+1}) + O(\Delta \xi^4) \end{cases} \tag{20}$$

$$\begin{cases} \frac{\partial u}{\partial \xi}|_{i-3/2} = \frac{1}{\Delta \xi}(\frac{71}{1920}u_{i-3} - \frac{141}{128}u_{i-2} + \frac{69}{64}u_{i-1} + \frac{1}{192}u_i - \frac{3}{128}u_{i+1} + \frac{3}{640}u_{i+2}) + O(\Delta \xi^5) \\ \frac{\partial u}{\partial \xi}|_{i-1/2} = \frac{1}{\Delta \xi}(-\frac{3}{640}u_{i-3} + \frac{25}{384}u_{i-2} - \frac{75}{64}u_{i-1} + \frac{75}{64}u_i - \frac{25}{384}u_{i+1} + \frac{3}{640}u_{i+2}) + O(\Delta \xi^5) \\ \frac{\partial u}{\partial \xi}|_{i+1/2} = \frac{1}{\Delta \xi}(-\frac{3}{640}u_{i-3} + \frac{3}{128}u_{i-2} - \frac{1}{192}u_{i-1} - \frac{69}{64}u_i + \frac{141}{128}u_{i+1} - \frac{71}{1920}u_{i+2}) + O(\Delta \xi^5) \end{cases} \tag{21}$$

The other terms are determined similarly. For comparison, the terms used in Ref.[13, 14] by De Rango and Zingg etal are given as the following,

$$\begin{cases} \mu_{i-3/2} = \frac{1}{16}(-\mu_{i-3} + 9\mu_{i-2} + 9\mu_{i-1} - \mu_i) + O(\Delta \xi^4) \\ \mu_{i-1/2} = \frac{1}{16}(\mu_{i-2} + 9\mu_{i-1} + 9\mu_i - \mu_{i+1}) + O(\Delta \xi^4) \\ \mu_{i+1/2} = \frac{1}{16}(\mu_{i-1} + 9\mu_i + 9\mu_{i+1} - \mu_{i+2}) + O(\Delta \xi^4) \end{cases} \tag{22}$$

$$\begin{cases} \frac{\partial u}{\partial \xi}|_{i-3/2} = \frac{1}{24\Delta \xi}(-u_{i-3} - 27u_{i-2} + 27u_{i-1} - u_i) + O(\Delta \xi^4) \\ \frac{\partial u}{\partial \xi}|_{i-1/2} = \frac{1}{24\Delta \xi}(-u_{i-2} - 27u_{i-1} + 27u_i - u_{i+1}) + O(\Delta \xi^4) \\ \frac{\partial u}{\partial \xi}|_{i+1/2} = \frac{1}{24\Delta \xi}(-u_{i-1} - 27u_i + 27u_{i+1} - u_{i+2}) + O(\Delta \xi^4) \end{cases} \tag{23}$$

Compare Eqs.(20),(21) and Eqs.(22),(23), it can be seen that μ_I in present paper has the same accuracy order, as that of De Rango and Zingg et al, but has small stencil width $(i-2,\cdots,i+1)$, $\frac{\partial u}{\partial \xi}|_I$ has the same stencil width, but obtains one accuracy order higher than that in Ref.[13, 14].

Table 1: The coefficients of C_l^I

I	C_{-2}^I	C_{-1}^I	C_0^I	C_1^I
$i-3/2$	5/16	15/16	-5/16	1/16
$i-1/2$	-1/16	9/16	9/16	-1/16
$i+1/2$	1/16	-5/16	15/16	5/16

Table 2: The coefficients of D_l^I

I	D_{-3}^I	D_{-2}^I	D_{-1}^I	D_0^I	D_1^I	D_2^I
$i-3/2$	71/1920	-141/128	69/64	1/192	-3/128	3/640
$i-1/2$	-3/640	25/384	-75/64	75/64	-25/384	3/640
$i+1/2$	-3/640	3/128	-1/192	-69/64	141/128	-71/1920

Table 3: The coefficients of C_l^c

C_{-2}^c	C_{-1}^c	C_0^c	C_1^c	C_2^c
1/12	-8/12	0	8/12	-1/12

It can be proved that the scheme Eq. (8) is symmetric with respect to cell i. For example, the coefficients of $\mu_{i-2}u_{i-3}$, $\mu_{i+2}u_{i+3}$, $\mu_{i-1}u_{i-2}$, and $\mu_{i+1}u_{i+2}$ can be found as (in the following formula, $\tilde{C}_l^I$ and $\tilde{D}_l^I$ are the coefficients of μ_{i+l}, u_{i+l} in R_I for $\tilde{R}_{i+1/2}$, respectively. It's clear that there are $\tilde{C}_l^I = C_{l-1}^{I-1}$ and $\tilde{D}_l^I = D_{l-1}^{I-1}$, $\tilde{\alpha}_I = \alpha_{I-1}$, $I = i-1/2, i+1/2, i+3/2$):

$$
\begin{aligned}
C_{i-2,i-3} &= -\textstyle\sum_{I=i-3/2}^{i+1/2} \alpha_I C_{-2}^I D_{-3}^I \\
&= -\left[(\tfrac{-1}{24})\cdot\tfrac{5}{16}\cdot\tfrac{71}{1920} + \tfrac{26}{24}\cdot(\tfrac{-1}{16})\cdot(\tfrac{-3}{640}) + (\tfrac{-1}{24})\cdot\tfrac{1}{16}\cdot(\tfrac{-3}{640})\right] \\
&= \tfrac{7}{46080} \\
C_{i+2,i+3} &= \textstyle\sum_{I=i-1/2}^{i+3/2} \tilde{\alpha}_I \tilde{C}_2^I \tilde{D}_3^I \\
&= (\tfrac{-1}{24})\cdot\tfrac{1}{16}\cdot\tfrac{3}{640} + \tfrac{26}{24}\cdot(\tfrac{-1}{16})\cdot\tfrac{3}{640} + (\tfrac{-1}{24})\cdot\tfrac{5}{16}\cdot(\tfrac{-71}{1920}) \\
&= \tfrac{7}{46080} \\
C_{i-1,i-2} &= \textstyle\sum_{I=i-1/2}^{i+3/2} \tilde{\alpha}_I \tilde{C}_{-1}^I \tilde{D}_{-2}^I - \sum_{I=i-3/2}^{i+1/2} \alpha_I C_{-1}^I D_{-2}^I \\
&= (\tfrac{-1}{24})\cdot\tfrac{5}{16}\cdot\tfrac{71}{1920} + \tfrac{26}{24}\cdot(\tfrac{-1}{16})\cdot(\tfrac{-3}{640}) + (\tfrac{-1}{24})\cdot\tfrac{1}{16}\cdot(\tfrac{-3}{640}) \\
&\quad -\left[(\tfrac{-1}{24})\cdot\tfrac{15}{16}\cdot(\tfrac{-141}{128}) + \tfrac{26}{24}\cdot\tfrac{9}{16}\cdot\tfrac{25}{384} + (\tfrac{-1}{24})\cdot(\tfrac{-5}{16})\cdot\tfrac{3}{128}\right] \\
&= -\tfrac{479}{5760} \\
C_{i+1,i+2} &= \textstyle\sum_{I=i-1/2}^{i+3/2} \tilde{\alpha}_I \tilde{C}_1^I \tilde{D}_2^I - \sum_{I=i-3/2}^{i+1/2} \alpha_I C_1^I D_2^I \\
&= (\tfrac{-1}{24})\cdot(\tfrac{-5}{16})\cdot(\tfrac{-3}{128}) + \tfrac{26}{24}\cdot\tfrac{9}{16}\cdot(\tfrac{-25}{384}) + (\tfrac{-1}{24})\cdot\tfrac{15}{16}\cdot\tfrac{141}{128} \\
&\quad -\left[(\tfrac{-1}{24})\cdot\tfrac{1}{16}\cdot\tfrac{3}{640} + \tfrac{26}{24}\cdot(\tfrac{-1}{16})\cdot\tfrac{3}{640} + (\tfrac{-1}{24})\cdot\tfrac{5}{16}\cdot(\tfrac{-71}{1920})\right] \\
&= -\tfrac{479}{5760}
\end{aligned}
$$

So we have $C_{i-2,i-3} = C_{i+2,i+3}$, $C_{i-1,i-2} = C_{i+1,i+2}$, and so on. Hence the scheme Eq. (8) is symmetric with respect to grid node i. The symmetry of central differencing for Eq. (8) satisfies the diffusion property of the viscous flux.

Next, we prove that the order of accuracy given by Eq.(11) is satisfied. Take the term $T^- = \mu\partial u/\partial\xi$ in Eq.(11) as the example,

In $\tilde{R}_{i-1/2}$, at $I = i - 3/2$, based on Taylor's series expansion

$$\begin{aligned} T^-_{i-3/2} = \textstyle\sum_{l=m}^{n} C_l^I \mu_{i+l} (\frac{1}{\Delta\xi} \sum_{l=r}^{s} D_l^I u_{i+l}) &= \left[\mu_{i-3/2} + A_I \mu^{(4)}_{i-3/2} \Delta\xi^4 + O(\Delta\xi^5)\right] \left[\tfrac{\partial u}{\partial\xi}|_{i-3/2} + O(\Delta\xi^5)\right] \\ &= \mu_{i-3/2} \tfrac{\partial u}{\partial\xi}|_{i-3/2} + A_I \mu^{(4)}_{i-3/2} \tfrac{\partial u}{\partial\xi}|_{i-3/2} \Delta\xi^4 + O(\Delta\xi^5) \end{aligned}$$

A_I is the coefficient of Taylor's series expansion.

The corresponding term T^+ in $\tilde{R}_{i+1/2}$ is at $I = i - 1/2$, and

$$\begin{aligned} T^+_{i-1/2} = \textstyle\sum_{l=m}^{n} \tilde{C}_l^I \mu_{i+1+l} (\frac{1}{\Delta\xi} \sum_{l=r}^{s} \tilde{D}_l^I u_{i+1+l}) &= \left[\mu_{i-1/2} + \tilde{A}_I \mu^{(4)}_{i-1/2} \Delta\xi^4 + O(\Delta\xi^5)\right] \left[\tfrac{\partial u}{\partial\xi}|_{i-1/2} + O(\Delta\xi^5)\right] \\ &= \mu_{i-1/2} \tfrac{\partial u}{\partial\xi}|_{i-1/2} + \tilde{A}_I \mu^{(4)}_{i-1/2} \tfrac{\partial u}{\partial\xi}|_{i-1/2} \Delta\xi^4 + O(\Delta\xi^5) \end{aligned}$$

Note that $A_I = \tilde{A}_I$, hence

$$T^+_{i-1/2} - T^-_{i-3/2} = \mu_{i-1/2} \frac{\partial u}{\partial\xi}|_{i-1/2} - \mu_{i-3/2} \frac{\partial u}{\partial\xi}|_{i-3/2} + O(\Delta\xi^5)$$

The other two terms can be analyzed similarly as above, then Eq.(11)

$$\frac{1}{\Delta\xi}(\tilde{R}_{i+1/2} - \tilde{R}_{i-1/2}) = R^{'}(\xi_i) + O(\Delta\xi^4)$$

is proved, i.e. the constructed schemes are formally 4th order accuracy.

2.4 Structural Model

For the computation of the vortex-induced oscillating cylinder, which is elastically supported as shown in Fig. 1 so that it oscillates only in the direction aligned with or normal to the incoming flow, the structural dynamic equations that governs the motion of the cylinder are:

$$m\ddot{x} + C_x\dot{x} + K_x x = D_f \tag{24}$$

$$m\ddot{y} + C_y\dot{y} + K_y y = L_f \tag{25}$$

These equations are solved implicitly together with the equations of flow motion in a fully coupled manner. In Eq. (24), $\ddot{x}$, $\dot{x}$, and x represent the dimensionless horizontal acceleration, velocity and displacement of the moving object respectively. Similarly, $\ddot{y}$, $\dot{y}$, and y in Eq. (25) represent the acceleration, velocity and displacement in the vertical direction. The terms m, L_f, and D_f are the mass, lift, and drag per unit span respectively, C_x and C_y are the damping coefficients in horizontal and vertical directions, and K_x and K_y are the spring constants in horizontal and vertical directions. In the present study, this 'self-excited oscillators' is assumed to have the same response in both directions, i.e. $C_x = C_y$ and $K_x = K_y$.

If the normalization procedure is applied to Eqs. (24) and (25) by using the same reference scales of those used for the equations of flow motion, the following nondimensional equations are obtained:

$$\ddot{x} + 2\zeta \left(\frac{2}{\bar{u}}\right) \dot{x} + \left(\frac{2}{\bar{u}}\right)^2 x = \frac{2}{\mu_s \pi} C_d \tag{26}$$

$$\ddot{y} + 2\zeta\left(\frac{2}{\bar{u}}\right)\dot{y} + \left(\frac{2}{\bar{u}}\right)^2 y = \frac{2}{\mu_s \pi} C_l \tag{27}$$

where ζ is the nondimensional structural damping coefficient calculated by $\zeta = C_{x,y}/[2\sqrt{mK_{x,y}}]$, $\bar{u}$ is the reduced velocity defined by $\bar{u} = U_\infty/b\omega$, b is radius of the cylinder, $\omega = \sqrt{K_{x,y}/m}$, the mass ratio defined by $\mu_s = m/\pi\rho_\infty b^2$, and C_d and C_l are the drag and lift coefficients respectively. Then the equations are transformed to a state form and expressed by:

$$[\mathbf{M}]\frac{\partial\{\mathbf{S}\}}{\partial t} + [\mathbf{K}]\{\mathbf{S}\} = \mathbf{q} \tag{28}$$

where

$$\mathbf{S} = \begin{pmatrix} x \\ \dot{x} \\ y \\ \dot{y} \end{pmatrix}, \mathbf{M} = [I], \mathbf{K} = \begin{pmatrix} 0 & -1 & 0 & 0 \\ \left(\frac{2}{\bar{u}}\right)^2 & 2\zeta\left(\frac{2}{\bar{u}}\right) & 0 & 0 \\ 0 & 0 & 0 & -1 \\ 0 & 0 & \left(\frac{2}{\bar{u}}\right)^2 & 2\zeta\left(\frac{2}{\bar{u}}\right) \end{pmatrix}, \mathbf{q} = \begin{pmatrix} 0 \\ \frac{2}{\mu_s\pi} C_d \\ 0 \\ \frac{2}{\mu_s\pi} C_l \end{pmatrix}.$$

2.5 The Time Discretization[38, 39]

A pseudo temporal term $\frac{\partial Q}{\partial \tau}$ is added to the governing equation (5) for the unsteady calculation. The physical temporal term $\frac{\partial Q}{\partial t}$ is discretized implicitly using a 2nd-order three point, backward differencing as the following

$$\frac{\partial Q}{\partial t} = \frac{3Q^{n+1} - 4Q^n + Q^{n-1}}{2\Delta t},$$

and the pseudo temporal term is discretized with first-order Euler scheme to enhance diagonal dominance. The semi-discretized governing equation (5) can then be expressed as

$$[(\frac{1}{\Delta\tau} + \frac{1.5}{\Delta t})I - (\frac{\partial R}{\partial Q})^{n+1,m}]\delta Q^{n+1,m+1} = R^{n+1,m} - \frac{3Q^{n+1,m} - 4Q^n + Q^{n-1}}{2\Delta t}, \tag{29}$$

where n is the physical time level index, m is the iteration index within a physical time step, Δt and $\Delta\tau$ are the physical and pseudo time step, R is the net flux evaluated on a grid point, respectively. Eq. (29) is solved using the unfactored Gauss-Seidel line iteration[38, 42, 43].

To couple the structural equations with the equations of flow motion and solve them implicitly in each physical time step, Eq. (28) is discretized and integrated in a manner consistent with Eq. (29)

$$\left(\frac{1}{\Delta\tau}\mathbf{I} + \frac{1.5}{\Delta t}\mathbf{M} + \mathbf{K}\right)\delta S^{n+1,m+1} = -\mathbf{M}\frac{3\mathbf{S}^{n+1,m} - 4\mathbf{S}^n + \mathbf{S}^{n-1}}{2\Delta t} - \mathbf{K}\mathbf{S}^{n+1,m} + \mathbf{q}^{n+1,m+1} \tag{30}$$

where n is the physical time level index and m stands for the pseudo time index.

The detailed coupling procedure between the fluid and structural systems can be referred in Ref[39]. Within a physical time step, the structural motion and the flow field are unknown and are solved iteratively between the fluid and structural systems in a fully couple manner.

In our study, within each physical time step, 80 pseudo time steps are used with the L_2 Norm residual reduced by 8 order of magnitude.

3 Results and Discussion

3.1 Wall Boundary Layer

A steady state laminar supersonic boundary layer flow on an adiabatic flat plate is employed to validate the present methodology. The incoming Mach number is 2.0. The Reynolds number based on the length of the flat plate is 4.0×10^4. The Prandtl number of 1.0 is used in order to compare with the analytical solution. The computation domain is taken to be $[0, 2] \times [0, 1.6]$. The mesh size is 180×80, and the CFL number of 200 is used.

The velocity and temperature profiles shown in Figs. 2 and 3 indicate that both the numerical results agree excellently with the Blasius solution.

3.2 Stationary cylinder

The flow past a stationary cylinder is used as the unsteady flow validation case. The zoomed mesh near the cylinder is shown in Fig. 4. The baseline mesh dimensions are 120×80 in circumferential and radial directions. After intensive numerical experiments, the far field boundary is chosen to be located 20 diameters away from the center of the cylinder because the solution is not sensitive to the far field boundary at this range. The Reynolds number based on the free-stream condition and cylinder diameter is $\mathrm{Re} = 500$.

The computed drag and lift coefficients are shown in Fig. 5. As shown in the figure, the lift oscillates at a certain frequency in terms of the Strouhal number St_{C_l}. The drag coefficient oscillates with twice that frequency, St_{C_d}. Table 4 shows that the results are in good agreement with the experiment [44, 45] and the results of other researchers[38, 39, 46]

Table 4: Results of refinement and comparison with the experiments

Mesh dimension	St_{C_d}	St_{C_l}	C_l	C_d
120×80	0.4573	0.2289	1.183	1.486
240×160	0.4539	0.2267	1.184	1.486
120×80 [38]	0.4126	0.2075	0.992	1.341
200×150 [38]	0.4199	0.2100	1.000	1.353
120×80 [39]	0.4395	0.2197	1.181	1.453
200×120 [39]	0.4516	0.2246	1.227	1.484
384×96 [46]	0.4674	0.2331	1.149	1.315
Roshko[44]		0.2075		
Goldstein[45]		0.2066		

Fig. 6 shows the comparison of the results with refined mesh 240×160. There is little difference between the results of the baseline mesh and refined mesh. This shows that the mesh system 120×80 is sufficient for this problem with $Re = 500$.

3.3 Vortex-induced-vibration of circular cylinder

After the stationary cylinder vortex shedding flow becomes dynamically stable, the cylinder is released to be controlled by the structure model as shown in Fig. 1. Same as the stationary cylinder case, a low Reynolds number, $\mathrm{Re} = 500$, is used. For the purpose of comparison with the experimental data of [47], several different combinations of structural parameters are used in the computation.

In this study, for all the cases of oscillating cylinder, Strouhal number is set to be 0.2, corresponding to $\bar{u} = 1.5915$. Different mass ratios, μ_s, are used to test the different responses of the structural system. They are equal to 1.2732, 5.0, and 12.7324, respectively. To match the wide range of the experimental data, the damping ratio, ζ, is varied in the range 0.001 - 1.583.

The numerical results for present study are plotted in Fig. 7 for the three values of μ_s. Also plotted are the computations conducted in [46] with $\mu_s = 5.0$, computations in [48] with $\mu_s = 12.73$, and the experimental data given in [47]. In the figure, the abscissa is the reduced damping coefficient with the form of $8\pi^2 \mathrm{St}^2 \zeta m/\rho D^2$ [49], and the ordinate is the cross-flow displacement of motion normalized by the diameter of the cylinder. Overall, a good agreement is observed between the present results and the experimental results. The low damping ratio case with $\mu_s = 1.2732$ shows better agreement with experiments. The results of $\mu_s = 5.0$ and $\mu_s = 12.7324$ are consistent with the numerical results conducted by other researchers.

Fig. 8 gives the comparison of the trajectories at the reduced damping coefficient of 2.0, the trajectories are similar to the results computed by [49] and [46].

Fig. 9 compares the time histories of the lift and drag coefficients at the reduced damping coefficient of 2.0. It can be seen that, with the increasing mass ratio μ_s, the amplitude of lift increases slightly, but drag amplitude increases significantly.

Fig. 10 gives the comparison of the trajectories with the same $\zeta = 0.1583$ at different mass ratio μ_s. When μ_s is decreased, the trajectory becomes more asymmetrical.

Fig. 11 compares the time histories of the lift and drag coefficients with $\zeta = 0.1583$ at different mass ratio μ_s. When μ_s is decreased, the lift decreases and the drag increases.

Fig. 12 gives the comparison of the trajectories for the same $\mu_s = 12.7324$ with different ζ. The trajectory of $\zeta = 0.001583$ is quite irregular due to the smaller damping constrain. When ζ is increased, the amplitude of vibration is decreased.

Fig. 13 compares the time histories of the lift and drag coefficients for $\mu_s = 12.7324$ with different ζ. Similar to the results of Fig. 11, the increased ζ leads to the lift increase and the drag decrease.

4 Conclusion

A set of fully conservative 4th-order central differencing schemes for the viscous terms of Navier-Stokes equations are proved in this paper. These schemes are used with the 5th order WENO schemes for inviscid flux. The stencil width of the central differencing scheme is within that of the WENO scheme. The algorithm is used to simulate the vortex-induced oscillations of an elastically mounted circular cylinder.

The conservative 4th order viscous schemes have the following feature:

(1) For the viscous flux at an interface, all the terms at the the associated interfaces are evaluated using the same points. This guarantees the maximum order of accuracy;

(2) The schemes are symmetric central differencing with respect to the grid node. The symmetry satisfies the diffusion property of the viscous flux.

The schemes are validated with the flow of supersonic plate boundary layer flow and the flow past a stationary cylinder. Excellent agreement with theoretical results and experiment are obtained.

The algorithm then is employed to simulate the vortex-induced-vibration of a circular cylinder. The variation of lift coefficient, drag coefficient, and trajectory under different conditions are compared. If the reduced damping or the structural damping coefficient is given, the larger the mass ratio, the smaller the amplitude. With the increased mass ratio, the amplitude of lift increases slightly, but the drag amplitude increases significantly. If a mass ratio is specified, the smaller damping coefficient induces more irregular

trajectory. The increased damping coefficient leads to lift increase and drag decrease. The computed cylinder vibration displacement is in good agreement with experiment.

5 Acknowledgment

This work is supported by AFOSR Grant FA9550-06-1-0198 monitored by Dr Fariba Fahroo, and is supported by Miami Wind ^{TM} at University of Miami.

References

[1] J. A. Ekaterinaris, "High-order accurate, low numerical diffusion methods for aerodynamics," *Progress in Aerospace Sciences*, vol. 41, pp. 192–300, 2005.

[2] Z. J. Wang, "High-order methods for the Euler and Navier-Stokes equations on unstructured grids," *Progress in Aerospace Sciences*, vol. 43, pp. 1–41, 2007.

[3] A. Harten, B. Engquist, S. Osher, and S. Chakravarthy, "Uniformly High Order Essentially Non-Oscillatory Schemes, III," *Journal of Computational Physics*, vol. 71, pp. 231–303, 1987.

[4] C.-W. Shu and O. Osher, "Efficient Implementation of Essentially Non-Oscillatory Shock Capturing Schemes," *Journal of Computational Physics*, vol. 77, pp. 439–471, 1988.

[5] G.S. Jiang, and C.W. Shu, "Efficient implementation of weighted ENO schemes," *J.Comput.Phys.*, vol. 126, pp. 202–228, 1996.

[6] C.W. Shu, "Essentially non-oscillatory and weighted essentially non-oscillatory schemes for hyperbolic conservation laws." NASA/CR-97-206253, ICASE Report No.97-65, Nov. 1997.

[7] D.S. Balsara and C.-W. Shu, "Monotonicity Preserving weighted essentially non-oscillatory schemes with increasingly high order of accuracy," *J.Comput.Phys.*, vol. 160, pp. 405–452, 2000.

[8] Y. Shen, G. Zha, " Improvement of the WENO Scheme Smoothness Estimator." aiaa-2008-3993, 2008.

[9] Y.Q. Shen, G.C. Zha, and B.Y. Wang, "Improvement of the stability and accuracy of implicit WENO scheme for transonic flows." AIAA-paper 2007-4431, Submitted to AIAA J., 2008.

[10] V.A. Titarev, E.F. Toro, "Finite-volume WENO schemes for three-dimensional conservation laws," *J.Comput.Phys.*, vol. 201, pp. 238–260, 2004.

[11] T. Zhou, Y. Li, C.W. Shu, "Numerical comparison of WENO finite volume and Runge-Kutta discontinuous Galerkin methods," *J.Sci.Comput.*, vol. 16, pp. 145–171, 2001.

[12] S. A. Lele, "Compact Finite Difference Schemes with Spectral-like Resolution," *Journal of Computational Physics*, vol. 103, No. 1, pp. 16–42, 1992.

[13] S. De Rango and D. W. Zingg, " Aerodynamic computations using a higher-order algorithm ." AIAA 99-0167, 1999.

[14] D. W. Zingg, S. De Rango, M. Nemec and T. H. Pulliam, "Comparison of Several Spatial Discretizations for the Navier-Stokes Equations," *Journal of Computational Physics*, vol. 160, pp. 683–704, 2000.

[15] Y.Q. Shen, B.Y. Wang,and G.C. Zha, "Implicit WENO scheme and high order viscous formulas for compressible flows." AIAA-paper 2007-4431, June 2007.

[16] T. Sarpkaya, " A critical review of the intrinsic nature of vortex-induced vibrations ," *Journal of Fluids and Structures* , vol. 19, pp. 389–447, 2004.

[17] C.H.K. Williamson and R. Govardhan, "Vortex-induced vibrations," *Annual Review of Fluid Mechanics*, vol. 36, pp. 413–455, 2004.

[18] C.H.K. Williamson and R. Govardhan, "A brief review of recent results in vortex-induced vibrations," *Journal of Wind Engineering and Industrial Aerodynamics, doi:10.1016/j.jweia.2007.06.019*, 2007.

[19] H. Al Jamal and C. Dalton, "The contrast in phase angles between forced and self-excited oscillations of a circular cylinder," *Journal of Fluids and Structures* , vol. 20, pp. 467–482, 2005.

[20] R.D. Gabbai and H. Benaroya, "An overview of modeling and experiments of vortex-induced vibration of circular cylinders," *Journal of Sound and Vibrations*, vol. 282, pp. 575–616, 2005.

[21] S. Meynen, H. Verma, P. Hagedorn and M. Schafer, "On the numerical simulation of vortex-induced vibrations of oscillating conductors," *Journal of Fluids and Structures* , vol. 21, pp. 41–48, 2005.

[22] S. Mittal, A. Raghuvanshi, "Control of vortex shedding behind circular cylinder for flows at low Reynolds numbers," *International Journal for Numerical Methods in Fluids*, vol. 35, pp. 421–447, 2001.

[23] S. Mittal, V. Kumar, "Flow-Induced vibrations of a light circular cylinder at Reynolds numbers 10^3 to 10^4 ," *Journal of Sound and Vibration*, vol. 245, pp. 923–946, 2001.

[24] T.K. Prasanth, S. Behara, S.P. Singh, R. Kumar and S. Mittal, "Effect of blockage on vortex-induced vibrations at low Reynolds numbers," *Journal of Fluids and Structures*, vol. 22, pp. 865–876, 2006.

[25] H.M. Blackburn and R.D. Henderson, "A study of the two-dimensional flow past an oscillating cylinder," *Journal of Fluid Mechanics*, vol. 385, pp. 255–286, 1999.

[26] H.M. Blackburn, R.N. Govardhan and C.H.K. Williamson, "A complementary numerical and physical investigation of vortex-induced," *Journal of Fluids and Structures*, vol. 15, pp. 481–488, 2000.

[27] C. Evangelinos, D. Lucor and G.E. Karniadakis, "DNS-derived force distribution on flexible cylinders subject to vortex-induced vibration," *Journal of Fluids and Structures* , vol. 14, pp. 429–440, 2000.

[28] D. Lucor, J. Foo and G.E. Karniadakis, "Vortex mode selection of a rigid cylinder subject to VIV at low mass-damping," *Journal of Fluids and Structures* , vol. 20, pp. 483–503, 2005.

[29] S. Dong and G.E. Karniadakis, "DNS of flow past a stationary and oscillating cylinder at Re=10,000," *Journal of Fluids and Structures* , vol. 20, pp. 519–531, 2005.

[30] J. B. V. Wanderley and C. A. Levi, "Validation of a finite difference method for the simulation of vortex-induced vibrations on a circular cylinder ," *Ocean Engineering*, vol. 29, pp. 445–460, 2002.

[31] K. Ryan, C.J. Pregnalato, M.C. Thompson and K. Hourigan, "Flow-induced vibrations of a tethered circular cylinder," *Journal of Fluids and Structures*, vol. 19, pp. 1085–1102, 2004.

[32] A. Placzek, J. F. Sigrist and A. Hamdouni, "Numerical simulation of an oscillating cylinder in a cross-flow at low Reynolds number: Forced and free oscillations," *Computers & Fluids, doi:10.1016/j.compfluid.2008.01.007*, 2008.

[33] E. Guilmineau and P. Queutey, "Numerical simulation of vortex-induced vibration of a circular cylinder with low mass damping," *Journal of Fluids and Structures* , vol. 19, pp. 449–466, 2004.

[34] E. Guilmineau and P. Queutey, "A numerical simulation of vortex shedding from an oscillating circular cylinder," *Journal of Fluids and Structures*, vol. 16, pp. 773–794, 2002.

[35] Z.Y. Pan, W.C. Cui and Q.M. Miao, "Numerical simulation of vortex-induced vibration of a circular cylinder at low mass-damping using RANS code," *Journal of Fluids and Structures* , vol. 23, pp. 23–37, 2007.

[36] M. Tutar and A.E. Holdo, "Large Eddy Simulation of a smooth circular cylinder oscillating normal to a uniform flow," *ASME Journal of Fluids Engineering*, vol. 122, pp. 694–702, 2000.

[37] H. Al Jamal and C. Dalton, "Vortex-induced vibrations using large eddy simulation at a moderate Reynolds number," *Journal of Fluids and Structures* , vol. 19, pp. 73–92, 2004.

[38] X.-Y. Chen, G.-C. Zha, and Z.-J. Hu, "Numerical Simulation of Flow Induced Vibration Based on Fully Coupled-Structural Interactions." AIAA Paper 2004-2240, AIAA 34th AIAA Fluid Dynamics Conference, 2004.

[39] X. Chen and G.-C. Zha, "Fully coupled fluid-structural interactions using an efficient high solution upwind scheme," *Journal of Fluid and Structure*, vol. 20, pp. 1105–1125, 2005.

[40] P. Thomas and C. Lombard, " Geometric Conservation Law and Its Application to Flow Computations on Moving Grids ," *AIAA Journal*, vol. 17, No. 10, pp. 1030–1037, 1979.

[41] Y.Q. Shen, G.C. Zha, and B.Y. Wang, "Improvement of the stability and accuracy of implicit WENO scheme for transonic flows." Submitted to AIAA J., 2007.

[42] Z.-J. Hu and G.-C. Zha, "Numerical Study on Flow Separation of a Transonic Cascade." AIAA Paper 2004-0199, Jan. 2004.

[43] Y.Q. Shen, B.Y. Wang,and G.C. Zha, "Comparison Study of Implicit Gauss-Seidel Line Iteration Method for Transonic Flows." AIAA-paper 2007-4332, June 2007.

[44] A. Roshko, "On the Development of Turbulent Wakes From Vortex Streets." NACA Rep. 1191, 1954.

[45] S. Goldstein, "Modern Developments in Fluid Dynamics." Clarendon Press, Oxford, 1938.

[46] J. Alonso, L. Martinelli, and A. Jameson, "Multigrid Unsteady Navier-Stokes Calculations with Aeroelastic Applications." AIAA Paper 95-0048, 1995.

[47] O. M. Griffin, "Vortex-induced vibrations of marine structures in uniform and sheared currents." NSF Workshopon Riser Dynamics, University of Michigan, 1992.

[48] S. A. Morton, R. B. Melville, and M. R. Visbal, "Accuracy and Coupling Issues of Aeroelastic Navier-Stokes Solutions on Deforming Meshes." AIAA Paper-97-1085, 1997.

[49] H. Blackburn and G. Karniadakis, "Two and Three-Dimensional Vortex-Induced Vibration of a Circular Cylinder." ISOPE-93 Conference, Singapore, 1993.

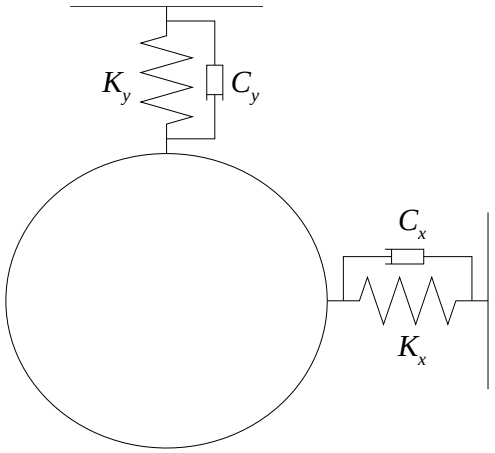

Figure 1: Sketch of the elastically mounted cylinder

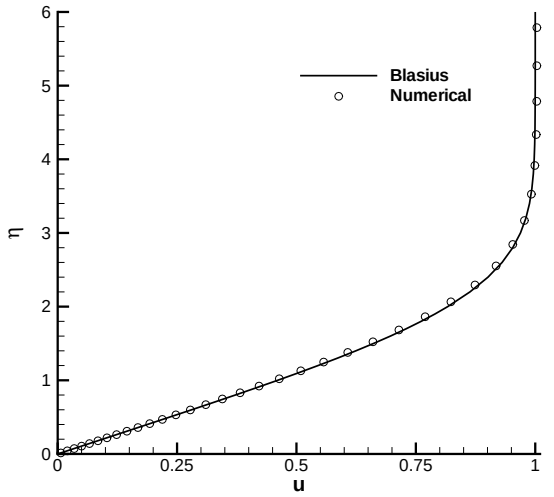

Figure 2: Comparison of the velocity profiles of the supersonic laminar boundary layer flows

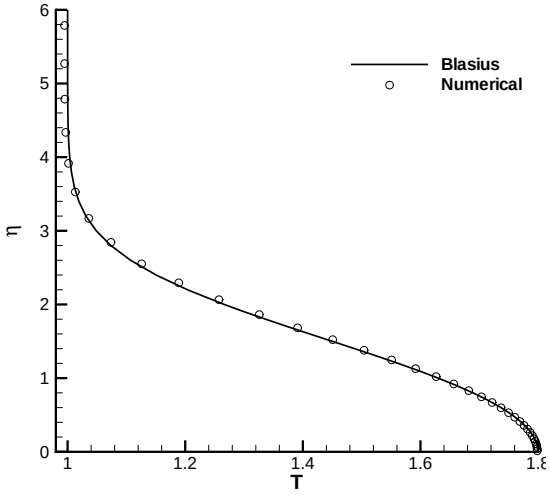

Figure 3: Comparison of the temperature profiles of the supersonic laminar boundary layer flows.

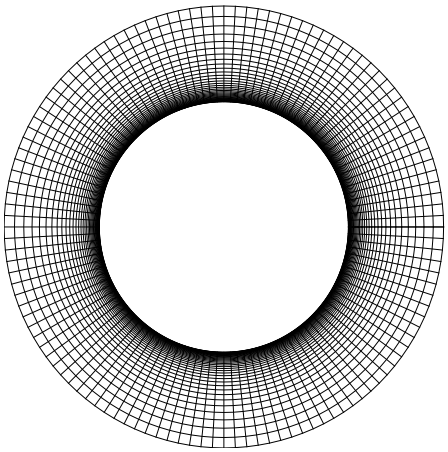

Figure 4: The near wall zone mesh around the solid surface of the cylinder

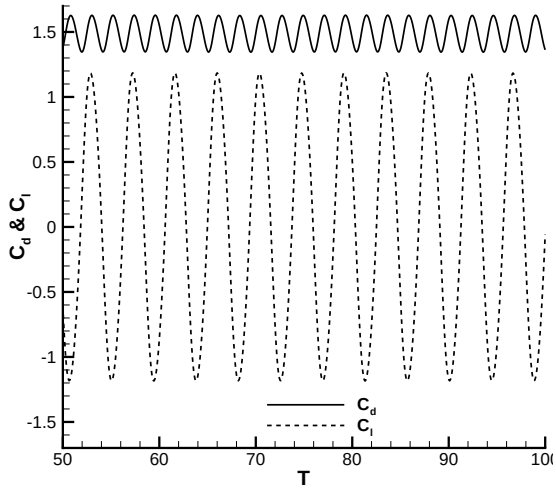

Figure 5: Time histories of the lift and drag coefficients of the stationary cylinder due to vortex shedding

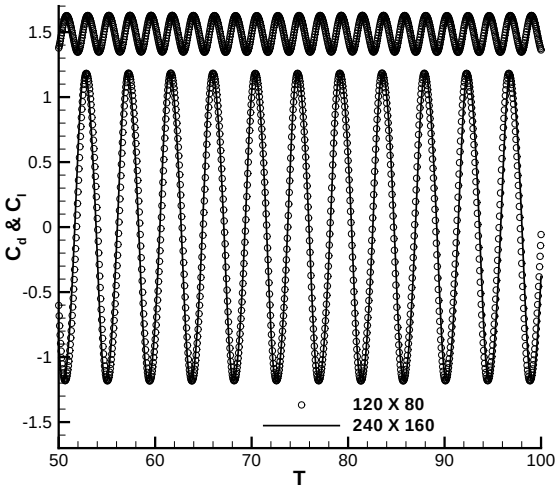

Figure 6: Comparison of two different mesh system, the stationary cylinder

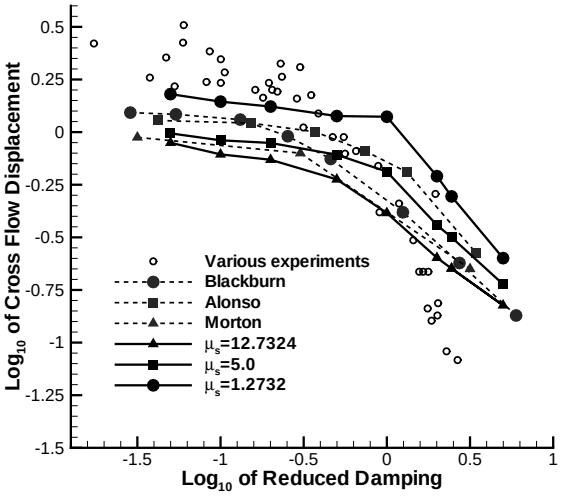

Figure 7: Comparison of the computed amplitude with Griffin's experimental data for the elastically mounted cylinder

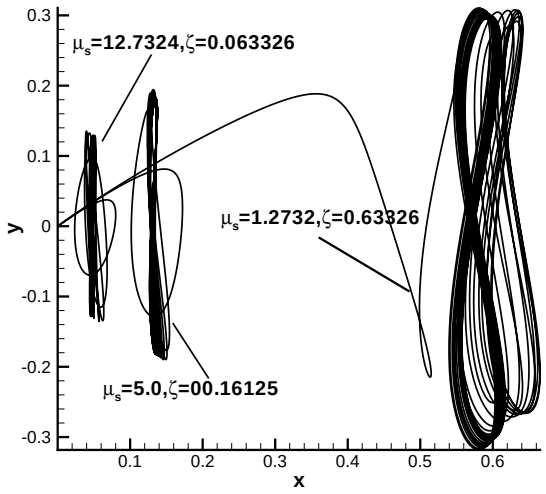

Figure 8: Comparison of the trajectories at the reduced damping 2.0

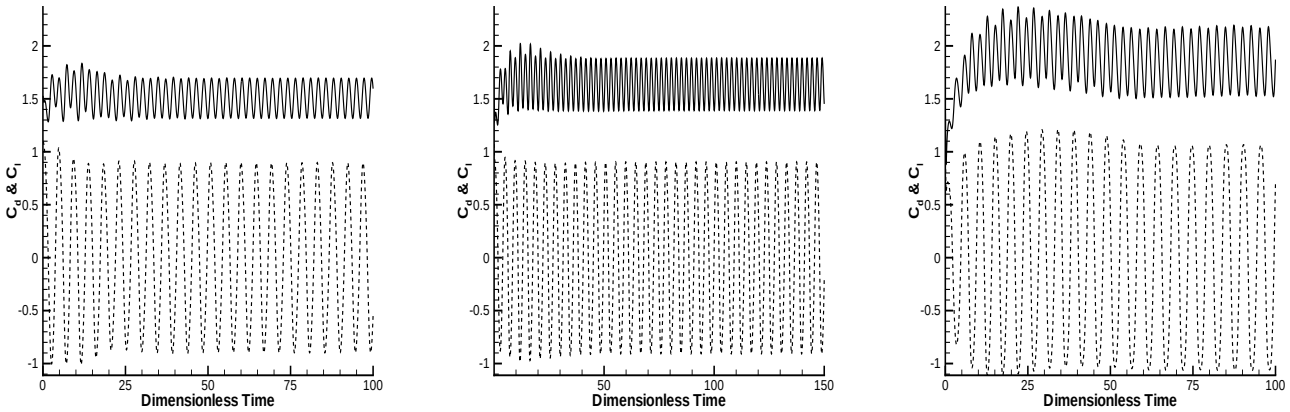

Figure 9: Comparison of the time histories of the lift and drag coefficients at the reduced damping 2.0. From left to right, $\mu_s = 12.7324$, $\mu_s = 5.0$, and $\mu_s = 1.2732$. C_d: Solid line, C_l: Dashed line

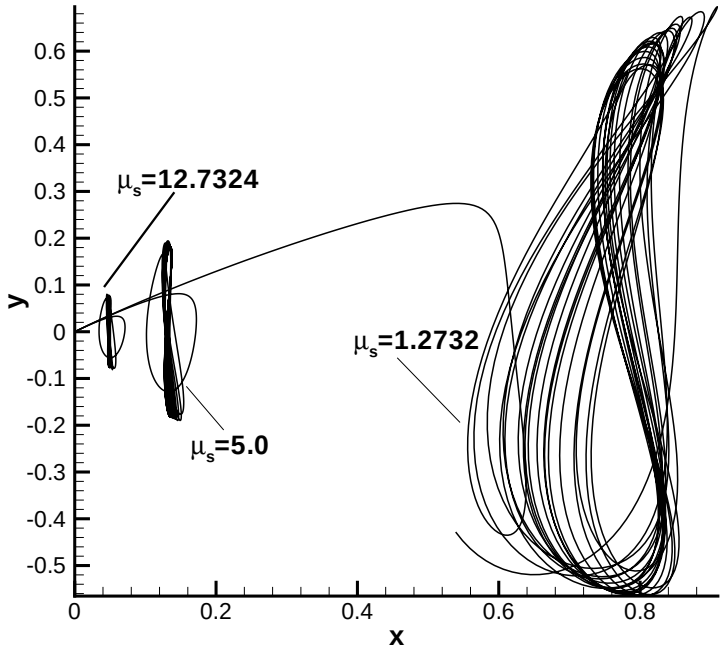

Figure 10: Comparison of trajectories with $\zeta = 0.1583$

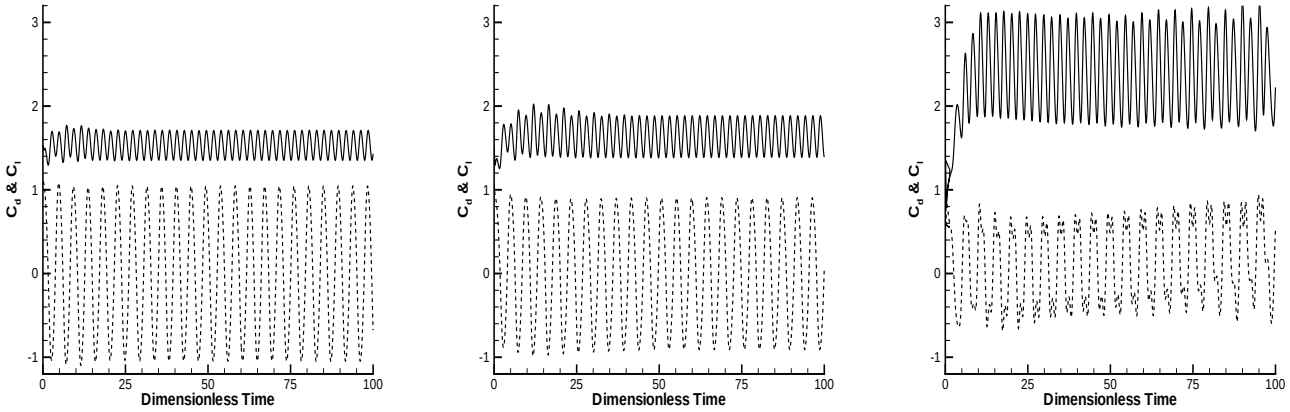

Figure 11: Comparison of the histories of the lift and drag coefficients with $\zeta = 0.1583$. From left to right, $\mu_s = 12.7324$, $\mu_s = 5.0$,and $\mu_s = 1.2732$. C_d: Solid line, C_l: Dashed line

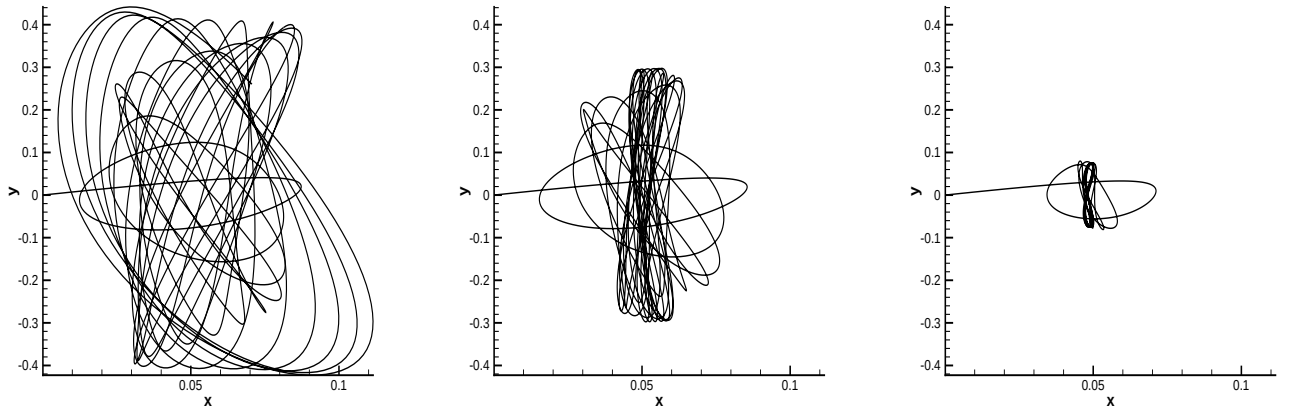

Figure 12: Comparison of the trajectories with $\mu_s = 12.7324$. From left to right, $\zeta = 0.001583$, $\zeta = 0.01583$, and$\zeta = 0.1583$

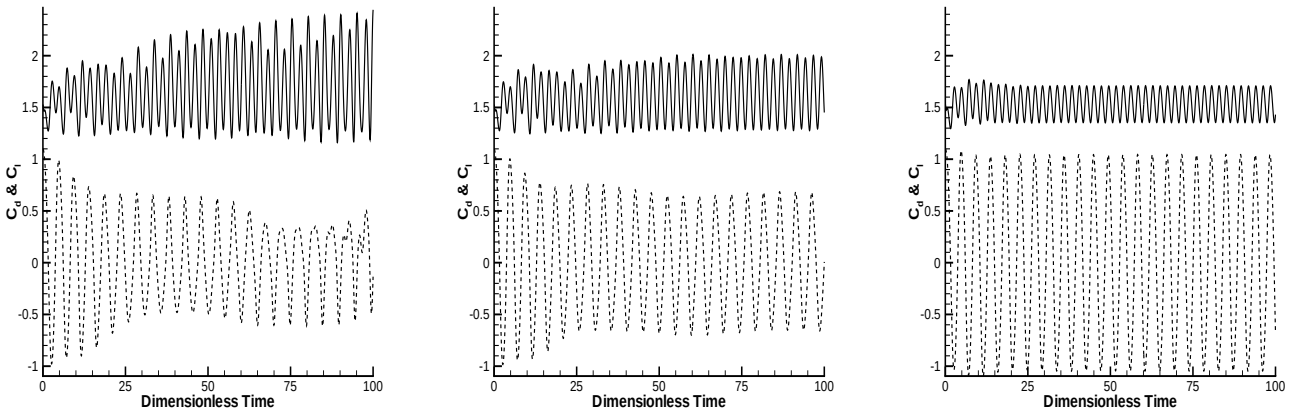

Figure 13: Comparison of the histories of the lift and drag coefficients with $\mu_s = 12.7324$. From left to right, $\zeta = 0.001583$, $\zeta = 0.01583$, and$\zeta = 0.1583$. C_d: Solid line, C_l: Dashed line